
TI-DeepONet: Learnable Time Integration for Stable Long-Term Extrapolation

Dibyajoti Nayak

Department of Civil and Systems Engineering
Johns Hopkins University
Baltimore, MD, 21218
dnayak2@jh.edu

Somdatta Goswami

Department of Civil and Systems Engineering
Johns Hopkins University
Baltimore, MD, 21218
somdatta@jhu.edu

Abstract

Accurate temporal extrapolation presents a fundamental challenge for neural operators in modeling dynamical systems, where reliable predictions must extend significantly beyond the training time horizon. Conventional deep operator network (DeepONet) approaches rely on two inherently limited training paradigms: fixed-horizon rollouts, which predict complete spatiotemporal solutions while disregarding temporal causality, and autoregressive formulations, which accumulate errors through sequential predictions in time. We introduce TI-DeepONet, a framework that integrates neural operators with adaptive numerical time-stepping techniques to preserve the underlying Markovian structure of dynamical systems while substantially mitigating error propagation in extended temporal forecasting. Our approach reformulates the learning objective from direct state prediction to the approximation of instantaneous time-derivative fields, which are subsequently integrated using established numerical schemes. This design naturally supports continuous-time prediction and enables the use of higher-precision integrators at inference than those employed during training, striking a balance between computational efficiency and predictive accuracy. We further develop TI(L)-DeepONet, which incorporates learnable coefficients for intermediate slopes in a multi-stage numerical integration scheme, thereby adapting to solution-specific variations and enhancing predictive fidelity. Rigorous evaluation across four canonical partial differential equations (PDEs) spanning diverse, high-dimensional, chaotic, dissipative, and dispersive dynamics shows that TI(L)-DeepONet marginally outperforms TI-DeepONet, with both frameworks achieving significant reductions in relative L_2 extrapolation error: approximately 81% compared to autoregressive implementations and 70% compared to fixed-horizon approaches. Notably, both methods maintain stable predictions over temporal domains extending to nearly twice the training interval. This research establishes a physics-aware operator learning paradigm that bridges neural approximation with numerical analysis principles, preserving the causal structure of dynamical systems while addressing a critical gap in long-term forecasting of complex physical phenomena.

1 Introduction

Time-dependent partial differential equations (PDEs) are typically solved using spatial discretization (e.g., finite element or volume) combined with time-stepping schemes such as Runge–Kutta or Adams–Bashforth. While accurate, such solvers can be prohibitively expensive for high-dimensional or many-query problems. Explicit integrators are constrained by stability conditions (e.g., CFL), while implicit schemes require solving large systems of equations at each step. Moreover, classical solvers generalize poorly: each new initial or boundary condition requires a fresh simulation.

Neural operators (NOs) offer an attractive alternative by learning mappings from input functions (e.g., initial conditions) to solutions, bypassing discretization and enabling fast inference. Models like DeepONet [1] and FNO [2] have shown promise in parametric PDE settings. However, extending NOs to time-evolving systems introduces new challenges. The standard approach is to train a model that maps the solution at time t to the solution at time $t + \Delta t$, and roll this forward autoregressively (see Figure 1). Unfortunately, this approach suffers from severe error accumulation, as each prediction feeds into the next, compounding inaccuracies and often leading to instability. Alternatively, one can train a model to predict an entire trajectory (“full rollout”), which avoids stepwise feedback but tends to degrade in accuracy when extrapolating beyond the training time window. Crucially, most existing works [3, 2, 4, 1] only evaluate models within the training time span, neglecting the need for reliable extrapolation, a capability that is essential for real-time engineering applications and control tasks. Moreover, existing work [5, 6, 7] on autoregressive and full rollout operator models tends to impose a discrete-time Markovian assumption, which misaligns with the underlying continuous-time dynamics of PDEs. These limitations often result in unstable or inaccurate long-term predictions. Thus, a key barrier remains: NOs struggle not only with long-horizon accuracy but also with extrapolating into unseen temporal domains, a prerequisite for trustworthy deployment.

Several recent works attempt to address these limitations. For example, Diab et al. [8] augment DeepONet with an additional temporal branch to capture dependencies, while Michalowska et al. [9] employ recurrent networks (RNNs, LSTMs, GRUs) atop neural operator outputs to better handle sequences. Other approaches introduce memory modules [10, 11, 12] to compensate for the non-Markovian nature of rollout-based methods. However, these strategies largely rely on generic time-series architectures rather than tackling the issue from a dynamical systems perspective.

In this work, we introduce a novel approach inspired by classical numerical analysis. Our proposed TI-DeepONet framework embeds time integration directly into the operator learning process for dynamical systems. Rather than predicting future solution states directly, we train a DeepONet to approximate the instantaneous time derivative $\partial u / \partial t$. During training, this derivative operator is coupled with a Runge-Kutta numerical integrator to evolve the state forward in time. The predicted future state is then compared against the ground truth in the loss function, enabling the network to learn dynamics that respect temporal causality and numerical stability. At inference time, we leverage high-order multistep integrators (such as Adams-Bashforth/Adams-Moulton predictor-corrector schemes) with refined timesteps to reliably propagate solutions based on the learned time derivative operator. This operator learning framework which maps between function spaces rather than from function spaces to vector spaces as in standard neural networks and neural ODEs [13] - provides the flexibility to modify time-stepping parameters between training and testing phases, thereby ensuring stable predictions. We further introduce TI(L)-DeepONet, an enhanced variant that incorporates learnable weighting coefficients conditioned on the system state at each timestep. This adaptation dynamically adjusts the integration process based on local solution characteristics.

While TI-DeepONet shares conceptual similarities with neural ODEs in learning time derivatives and using numerical integration, our approach differs significantly in both scope and implementation. Neural ODEs typically operate on low-dimensional latent states, whereas TI-DeepONet is specifically designed for high-dimensional spatiotemporal fields and learns an explicit operator mapping between function spaces. Furthermore, unlike neural ODEs, which treat the integrator as fixed, we explicitly embed the integrator within the solution operator, allowing us to employ different integration schemes at inference time according to accuracy and efficiency requirements.

We demonstrate the effectiveness of our approach on four benchmark PDEs: (1) 1D Burgers’, (2) 1D Korteweg-de Vries (KdV), (3) 1D Kuramoto-Sivashinsky (KS), and (4) 2D inviscid Burgers’ equations. We compare our methods against four standard neural operator (NO) baselines: (1) autoregressive DeepONet (DON AR), (2) full rollout DeepONet (DON FR), (3) autoregressive FNO (FNO AR), and (4) full rollout FNO (FNO FR). Across all cases, TI-DeepONet and its adaptive variant TI(L)-DeepONet significantly outperform standard autoregressive and full rollout operator models, achieving stable long-term predictions and accurate extrapolation for time horizons approximately twice as long as the training interval.

2 Methodology

We consider a general time-dependent PDE governing the spatiotemporal evolution of a solution field. Let the solution $u(\mathbf{x}, t)$ be defined over a temporal domain $t \in [0, T]$ and spatial domain $\mathbf{x} = [x_1, x_2, \dots, x_m] \in \mathcal{X} \subseteq \mathbb{R}^m$. The dynamics of u are governed by a PDE that relates the temporal derivative u_t to spatial derivatives $u_{\mathbf{x}}, u_{\mathbf{x}\mathbf{x}}, \dots$ via a general nonlinear function \mathcal{F} :

$$u_t = \mathcal{F}(t, \mathbf{x}, u, u_{\mathbf{x}}, u_{\mathbf{x}\mathbf{x}}, \dots). \quad (1)$$

This study examines the DeepONet framework to investigate error accumulation in autoregressive time-stepping, which serves as the primary motivation for this work. However, it should be noted that this error accumulation phenomenon is not limited to DeepONet but also occurs in other neural operator frameworks, such as FNO. To address this issue, we propose two novel architectures: TI-DeepONet and TI(L)-DeepONet. As will be shown later in this study in Sec. 3, these models effectively tackle this exact issue of autoregressive error accumulation. They are observed to significantly stabilize error growth and enable accurate long-term extrapolation. The following subsections provide a detailed introduction to these architectures.

2.1 Deep operator network (DeepONet)

Deep operator network (DeepONet) are grounded in the universal approximation theorem for nonlinear operators [14], and are designed to learn mappings between infinite-dimensional input and output function spaces. A standard DeepONet architecture comprises two subnetworks: a branch network and a trunk network. The branch network encodes the input function $\mathbf{v}(\eta)$, evaluated at a set of fixed sensor locations $\{\eta_1, \eta_2, \dots, \eta_m\}$, producing a set of coefficient weights. The trunk network takes as input the query coordinates $\zeta = (x, y, z, t)$ and outputs the corresponding basis functions.

The goal of DeepONet is to learn an operator $\mathcal{G}(\mathbf{v})$ such that, for any input realization \mathbf{v}_j , the output is a scalar-valued function evaluated at arbitrary spatiotemporal locations ζ . The predicted solution is computed as the weighted inner product of the outputs of the two networks defined as: $\mathcal{G}_{\theta}(\mathbf{v}_j)(\zeta) = \sum_{i=1}^p br_i(\mathbf{v}_j(\eta_1), \dots, \mathbf{v}_j(\eta_m)) \cdot tr_i(\zeta)$, where $br_i(\cdot)$ and $tr_i(\cdot)$ denote the outputs of the branch and trunk networks, respectively, and θ represents all trainable parameters.

In general, operator learning frameworks like DeepONet aim to learn a solution operator that maps any functional input, such as initial conditions (ICs), boundary conditions (BCs), or source terms, to the corresponding spatiotemporal solution field. However, this mapping is inherently non-causal with respect to time: the operator does not explicitly enforce the Markovian nature of dynamical systems, where the future state depends on the present (or past) states. As a result, direct operator prediction over time often fails to preserve temporal coherence, particularly for long-term simulations.

To account for temporal dynamics, a common strategy is to use autoregressive prediction, where the model recursively predicts the next state using the current state as input. This approach aligns more closely with the natural evolution of dynamical systems and is illustrated schematically in Fig. 1. However, autoregressive rollouts are prone to error accumulation and often degrade over long horizons - a core motivation for our proposed time-integrated operator learning framework.

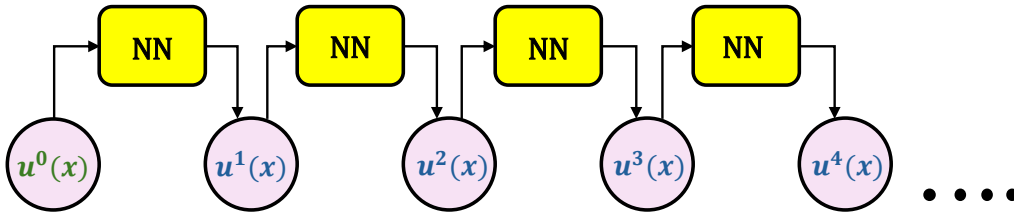


Figure 1: A schematic showing how autoregressive predictions in time are performed.

2.2 Time Integrator embedded deep operator network (TI-DeepONet)

As discussed previously, full spatiotemporal rollouts from a single-step operator such as vanilla DeepONet are not physically meaningful, as they disregard the temporal dependencies between

successive solution states. Additionally, autoregressive predictions suffer from error accumulation due to compounding approximation errors over time.

To mitigate these limitations, we propose the TI-DeepONet architecture. Rather than directly predicting the next state u^{i+1} , the network learns the right-hand side (RHS) of the time-dependent PDE (Eq. 1), i.e., the time derivative $u_t = \mathcal{F}(t, \mathbf{x}, u, u_{\mathbf{x}}, u_{\mathbf{x}\mathbf{x}}, \dots)$. This learned derivative is passed to a numerical time integrator to compute the next solution state from the current one. In particular, we use the RK4 scheme to advance the solution in time. For a timestep Δt , the RK4 update rule is given by, $k_1 = \mathcal{F}(t^i, u^i)$, $k_2 = \mathcal{F}(t^i + \frac{\Delta t}{2}, u^i + \frac{\Delta t}{2}k_1)$, $k_3 = \mathcal{F}(t^i + \frac{\Delta t}{2}, u^i + \frac{\Delta t}{2}k_2)$, $k_4 = \mathcal{F}(t^i + \Delta t, u^i + \Delta t \cdot k_3)$, and $u^{i+1} = u^i + \Delta t (\frac{1}{6}k_1 + \frac{2}{6}k_2 + \frac{2}{6}k_3 + \frac{1}{6}k_4)$. This formulation leads to an end-to-end differentiable pipeline, where the loss is computed between the predicted solution \hat{u}^{i+1} and the ground truth u^{i+1} , and gradients are backpropagated through the time integrator to update the network parameters. However, the RK4 slope coefficients, $\{\frac{1}{6}, \frac{2}{6}, \frac{2}{6}, \frac{1}{6}\}$, are fixed.

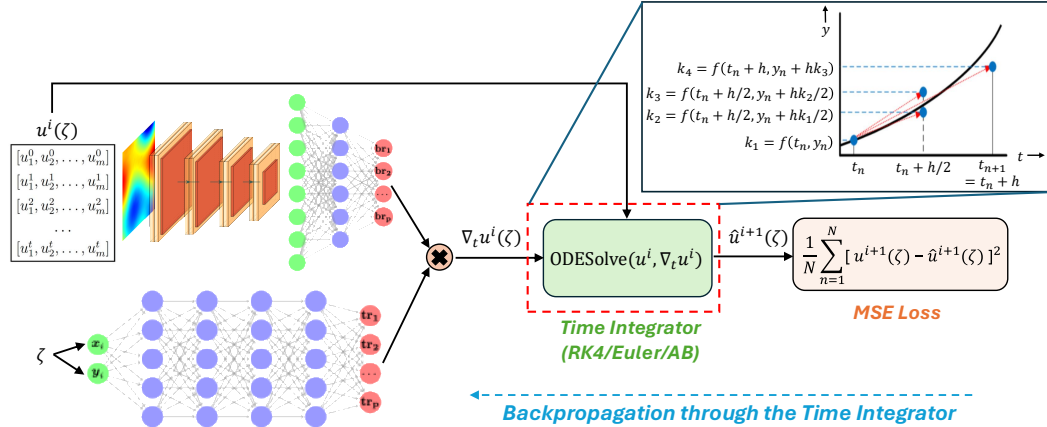


Figure 2: A schematic of the proposed TI-DeepONet architecture.

2.3 Learnable Time Integrator embedded deep operator network (TI(L)-DeepONet)

To introduce flexibility into the integration process, we extend TI-DeepONet by making the Runge–Kutta weighting coefficients learnable and state-dependent. This leads to the development of TI(L)-DeepONet. Specifically, we replace the constant RK4 slope coefficients, $\{\frac{1}{6}, \frac{2}{6}, \frac{2}{6}, \frac{1}{6}\}$, with adaptive coefficients conditioned on the current solution state u^i . We introduce an auxiliary neural network, NN_{RK} , which maps the current state to a set of four weights, $\alpha = [\alpha_1, \alpha_2, \alpha_3, \alpha_4] = \text{NN}_{\text{RK}}(u^i)$. These weights are then used to compute the next solution state via an adaptive RK4 update:

$$u^{i+1} = u^i + \Delta t \cdot (\alpha_1 k_1 + \alpha_2 k_2 + \alpha_3 k_3 + \alpha_4 k_4). \quad (2)$$

For numerical stability and interpretability, we normalize the weights using softmax activation function, such that: $\tilde{\alpha}_j = \frac{\exp(\alpha_j)}{\sum_{\ell=1}^4 \exp(\alpha_\ell)}$, $\forall j = 1, 2, 3, 4$. This adaptive scheme allows the model to adjust the influence of each intermediate slope dynamically, thereby compensating for the approximation error [15] of the DeepONet prediction, enabling more robust predictions in stiff, nonlinear, or highly transient regimes. For example, in regions with rapid spatial changes, the model may place greater weight on later-stage evaluations like k_4 , while in smoother regions, earlier evaluations may suffice.

3 Results

To evaluate the efficacy of our framework, we consider four canonical PDEs: (1) 1D Burgers' equation, (2) 1D KdV equation, (3) 1D KS equation, and (3) 2D inviscid Burgers' equation. Model performance is assessed using the relative L_2 error, defined as $\text{error} = \frac{\|u_{\text{pred}} - u_{\text{true}}\|_2}{\|u_{\text{true}}\|_2}$, where u_{pred} and u_{true} denote the predicted and ground truth solutions, respectively. Table 1 and Figure 3 summarize the comparative training and extrapolation accuracy across all methods for all applications. To evaluate the statistical variability of the performance of the model, we report the mean and standard deviation

of error metric in Table A2 based on five independent training trials. Additional details on data generation, training configurations, and network architecture are provided in Supplementary Information (SI) C. The code to reproduce the experiments is publicly available at <https://github.com/Centrum-IntelliPhysics/TI-DeepONet-for-Stable-Long-Term-Extrapolation.git>.

Table 1: Relative L_2 errors across frameworks in the extrapolation regime. TI-DeepONet AB employs RK4 during training and AB2/AM3 during inference. The **bold** values indicate the best-performing method at each time step, while the underlined values indicate the second-best.

Problem	t_{train}^*	Δt_e^*	Method	Relative L_2 error (in extrapolation)			
				$t+10\Delta t_e$	$t+20\Delta t_e$	$t+40\Delta t_e$	T^*
Burgers' (1D)	0.5	0.01	TI(L)-DON [Ours]	0.0204	0.0243	0.0377	0.0462
			TI-DON AB [Ours]	<u>0.0264</u>	<u>0.0310</u>	<u>0.0473</u>	<u>0.0579</u>
			DON Full Rollout	0.0433	0.0965	0.2413	0.3281
			DON Autoregressive	0.5898	0.8742	1.4682	1.7154
			FNO Full Rollout	0.2298	0.2521	0.2721	0.3551
			FNO Autoregressive	0.2377	0.2636	0.2790	0.2771
KdV (1D)	2.5	0.05	TI(L)-DON [Ours]	0.0522	0.0612	0.0701	0.1017
			TI-DON AB [Ours]	<u>0.0861</u>	<u>0.1114</u>	<u>0.1330</u>	<u>0.1941</u>
			DON Full Rollout	0.7769	0.7163	0.7197	0.7951
			DON Autoregressive	0.8127	0.8985	0.9691	1.0626
			FNO Full Rollout	0.8666	0.8040	0.7371	0.6352
			FNO Autoregressive	0.4171	0.4954	0.5501	0.5931
KS (1D)	15	0.3	TI(L)-DON [Ours]	0.0445	0.079	0.2056	0.3013
			TI-DON AB [Ours]	<u>0.0589</u>	<u>0.1066</u>	<u>0.2481</u>	<u>0.3366</u>
			DON Full Rollout	0.8298	0.8917	0.8482	0.9073
			DON Autoregressive	1.2744	1.2804	1.3204	1.3463
			FNO Full Rollout	0.9216	0.9468	0.8943	0.9292
			FNO Autoregressive	1.2246	1.2935	1.3207	1.3079
Inviscid Burgers' (2D)	0.33	0.01	TI(L)-DON [Ours]	<u>0.1838</u>	<u>0.2204</u>	0.2889	0.3207
			TI-DON AB [Ours]	0.1911	0.2288	<u>0.3003</u>	<u>0.3341</u>
			DON Full Rollout	0.3860	0.4406	0.5019	0.5232
			DON Autoregressive	0.7053	0.8589	1.1837	1.3495
			FNO Full Rollout	0.3095	0.3472	1.8104	2.2611
			FNO Autoregressive	0.0876	0.1729	0.4856	0.7214

* $t_{train} = t$: Beginning time of extrapolation; Δt_e : Evaluation timestep; T : Final prediction time.

3.1 One-dimensional Burgers' Equation

The viscous Burgers' equation is a canonical PDE arising in fluid mechanics, nonlinear acoustics, and traffic flow. For the velocity field $u(x, t)$ with viscosity $\nu = 0.01$, it is defined as:

$$\frac{\partial u}{\partial t} + u \frac{\partial u}{\partial x} = \nu \frac{\partial^2 u}{\partial x^2}, \quad (x, t) \in [0, 1] \times [0, 1], \quad (3)$$

with periodic BCs and IC, $u(x, 0) = s(x)$. We generated 2,500 realizations of $s(x)$ and the corresponding solutions, splitting them into 2,000 training and 500 test samples. To evaluate temporal extrapolation, models were trained on $t \in [0, 0.5]$ and tested on the full interval $t \in [0, 1]$.

In the full rollout setting, DeepONet learns a mapping $\mathcal{G}_\theta: s(x) \mapsto u(x, t)$ using a branch network (for the IC) and a trunk network (for spatiotemporal coordinates). A similar operator learning problem is defined for FNO. In this case, the mapping is also from the initial condition $s(x)$ to the full spatiotemporal solution field $u(x, t)$. The Fourier blocks in FNO employ an FNO2D-style architecture, applying the Fourier transform across both the x and t coordinates. A single forward pass

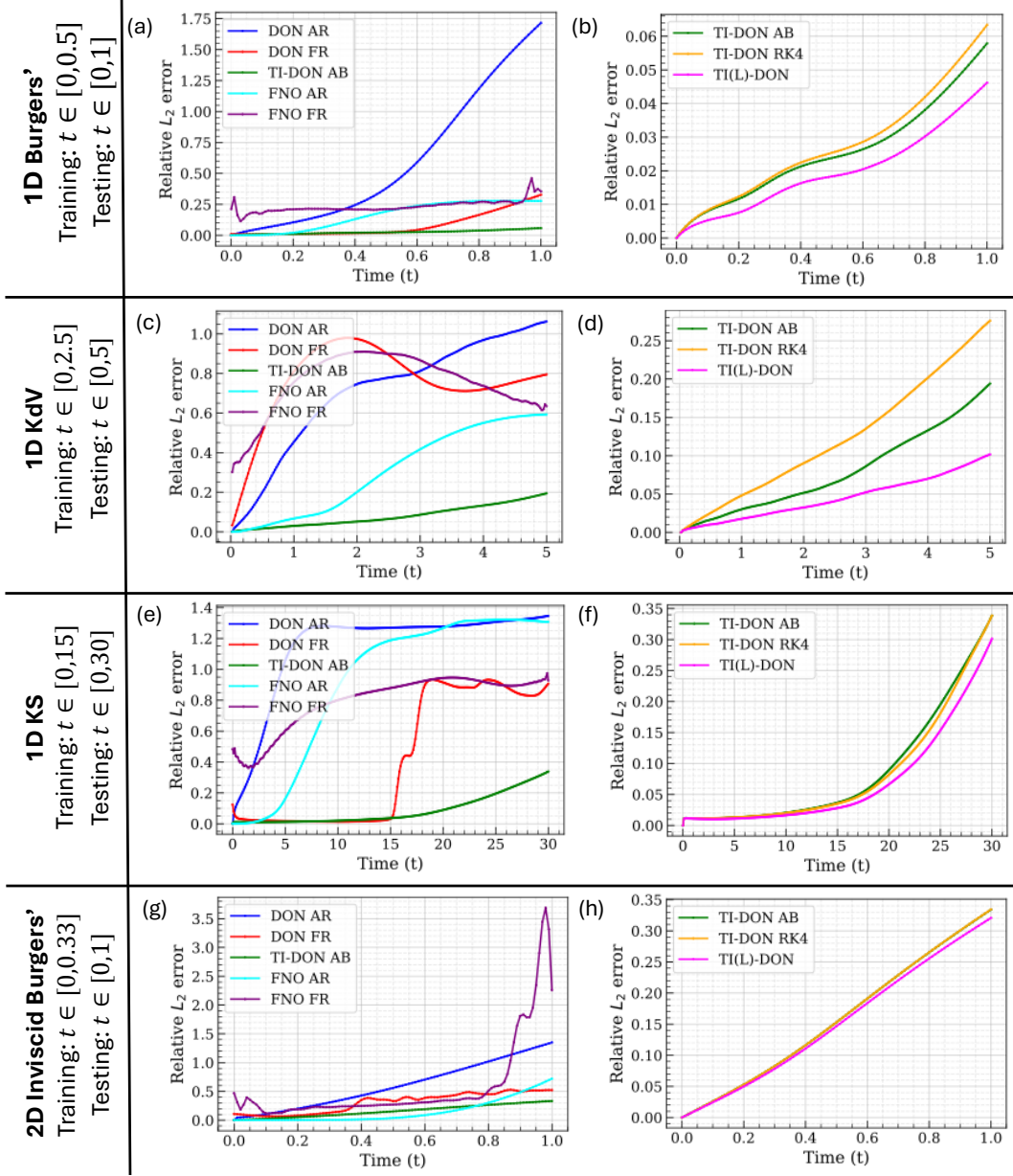


Figure 3: Temporal evolution of the relative L_2 error for different frameworks in all applications. Left: Comparison of baseline models with TI-DeepONet AB, which uses RK4 during training and AB2/AM3 during inference. Right: Comparison among TI-based variants. TI-DeepONet RK4 employs RK4 integration in both training and inference, while TI(L)-DeepONet adapts RK4 coefficients via a learnable scheme conditioned on the input state.

predicts the entire solution field. In the autoregressive setting, the models - Autoregressive DeepONet, TI-DeepONet, and TI(L)-DeepONet - the branch network takes as input the state of the system at the current timestep, and the trunk network takes only the spatial discretization. Autoregressive DeepONet predicts the solution at the next time step, while TI-DeepONet and TI(L)-DeepONet predict the time derivative of the solution at the current timestep and integrate temporal dynamics using numerical solvers. TI-DeepONet employs a Heun-type AB2/AM3 predictor-corrector scheme,

defined as:

$$\hat{u}^{n+1} = u^n + \Delta t \left[\frac{3}{2} \mathcal{F}(t^n, u^n) - \frac{1}{2} \mathcal{F}(t^{n-1}, u^{n-1}) \right], \quad (\text{Predictor}) \quad (4)$$

$$u^{n+1} = u^n + \Delta t \left[\frac{5}{12} \mathcal{F}(t^{n+1}, \hat{u}^{n+1}) + \frac{8}{12} \mathcal{F}(t^n, u^n) - \frac{1}{12} \mathcal{F}(t^{n-1}, u^{n-1}) \right] \quad (\text{Corrector}) \quad (5)$$

Lastly, in accordance with the autoregressive DeepONet learning, autoregressive FNO also operates in an analogous manner, where the mapping is defined as $\mathcal{G}_\theta: u(x, t) \mapsto u(x, t + 1)$. An FNO1D-style architecture is utilized in this case, applying the Fourier transform only in the x dimension.

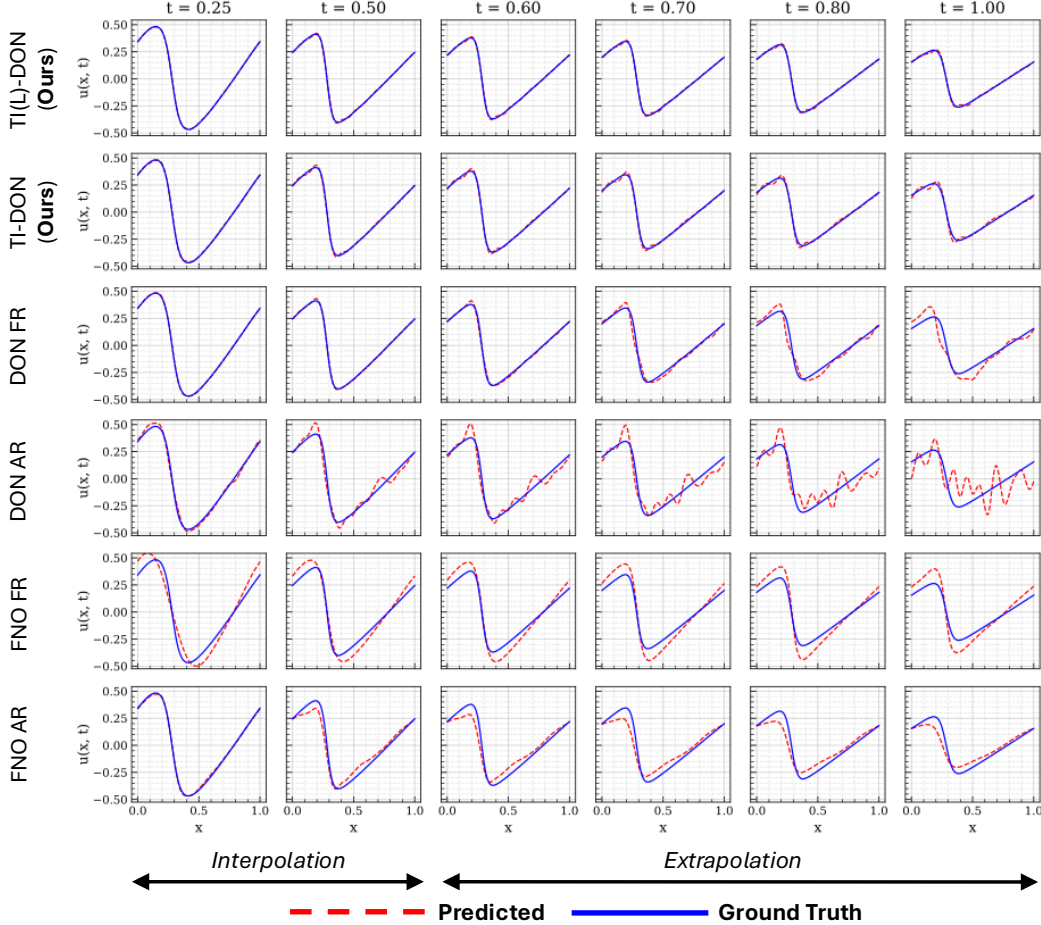


Figure 4: 1D Burgers' equation: Performance of all frameworks in the training ($t \in [0, 0.5]$) and extrapolation ($t \in [0.5, 1]$) regimes for a representative sample.

Figure 4 illustrates the performance of all models for a representative test sample. All models perform well within the training interval; however, the autoregressive DeepONet accumulates error early and diverges during extrapolation. The quantitative trends presented in Table 1 underscore the qualitative observations from Figure 4 as well as Figures 3(a) and (b). The autoregressive DeepONet deteriorates rapidly during extrapolation due to cumulative errors in the absence of stabilization mechanisms. While the full rollout DeepONet performs better owing to its non-recursive architecture, it fails to maintain accuracy beyond the training interval since it does not leverage the Markovian structure of time-dependent PDEs. Regarding the FNO variants, both full rollout and autoregressive FNO perform reasonably well within the training domain. However, in the extrapolation domain, both methods incur relatively higher errors, albeit lower than those of the autoregressive DeepONet. Notably, the autoregressive FNO does not exhibit the steep error growth observed in the autoregressive DeepONet during extrapolation. The full rollout FNO maintains higher errors throughout the entire temporal

domain, which can be attributed to its limited capacity to capture the full spectrum of frequencies in the system, as it is trained on solution information from only half of the temporal domain.

In contrast, the proposed TI-DeepONet variants, which embed numerical integration schemes into the learning framework, demonstrate superior extrapolation accuracy (see Figure 3(b)). TI-DeepONet with AB2/AM3 integration effectively stabilizes long-horizon predictions. TI(L)-DeepONet further improves on this by learning adaptive RK4 slope coefficients conditioned on the current state, enabling it to modulate time-stepping dynamically in response to the local solution behavior. This is particularly beneficial in stiff or nonlinear regimes, as reflected in the consistently lowest errors observed across all time steps. Figure A1 in SI presents iteration-wise learning of the RK4 slope coefficients, comparing it against the reference. An important point to note here is that the obtained optimized coefficients are compensating for the approximation error of the TI-DeepONet; hence, they may not necessarily adhere to the values obtained using the Taylor series expansion.

3.2 One-dimensional Korteweg-de Vries (KdV) Equation

The one-dimensional KdV equation models nonlinear dispersive waves and arises in contexts such as shallow water dynamics, plasma physics, and lattice acoustics. It introduces third-order dispersion into the Burgers-like formulation:

$$\frac{\partial u}{\partial t} - \eta u \frac{\partial u}{\partial x} + \gamma \frac{\partial^3 u}{\partial x^3} = 0, \quad (6)$$

where, u is the amplitude of the wave, γ and η are some real-valued scalar parameters, x and t are the spatial and temporal dimensions, respectively. We generated 1,000 initial conditions to simulate time evolution, splitting them into 800 for training and 200 for testing.

Figure 5 presents predictions from different frameworks on a representative sample. Both the full rollout and autoregressive DeepONet models fail to capture the dispersive, periodic dynamics of the solution. The full rollout approach, which treats time steps independently, lacks temporal continuity, while the autoregressive model suffers from compounding errors during recursive inference. Regarding the FNO variants, the full rollout FNO exhibits a noticeable phase shift due to its inability to capture the full spectrum of system frequencies; a consequence of being trained on a reduced temporal domain, thereby incurring significant errors throughout the entire temporal domain. The autoregressive FNO demonstrates particularly interesting behavior: while it achieves near-perfect predictions within the training domain, its performance deteriorates markedly upon entering the extrapolation regime. Here, autoregressive errors accumulate and manifest as spectral instability, characterized by frequency leakage. Specifically, the system’s frequencies become amplified at longer temporal horizons, resulting in erratic oscillations in the solution. Consequently, this approach also fails to reliably capture the inherent dispersive and periodic dynamics of the KdV PDE in the extrapolation domain. In contrast, TI-DeepONet and TI(L)-DeepONet closely match the ground truth, even in the extrapolation regime. The adaptive RK4 scheme in TI(L)-DeepONet yields similar accuracy as TI-DeepONet.

Figures 3(c) and (d) show the relative L_2 error over time. The autoregressive DeepONet exhibits rapid error growth beyond $t = 2.5$, while the full rollout model shows non-monotonic behavior due to its limited ability to model coherent temporal evolution. The full rollout FNO also exhibits a non-monotonic trend throughout the temporal domain, with the largest errors concentrated in the interval $t \in [1, 3]$. The autoregressive FNO achieves lower prediction errors within the training temporal domain but exhibits immediate steep error growth beyond $t = 2$. These quantitative L_2 error observations are in good agreement with the qualitative trends observed for the baselines in Figure 5. In comparison, the TI-based models maintain low and stable errors across the entire prediction window. At $t = 5$, TI(L)-DeepONet and TI-DeepONet achieve final errors of approximately 20% and 19.4%, respectively; 4-5 \times lower than baseline methods. The marginal performance difference between TI-DeepONet with AB2/AM3 and TI(L)-DeepONet indicates that both are reliable choices for long-term modeling of PDEs similar to the KdV equation.

3.3 One-dimensional Kuramoto-Sivashinsky (KS) Equation

The one-dimensional Kuramoto-Sivashinsky (KS) equation is a highly nonlinear PDE that is widely known for its chaotic behavior. It arises in various physical contexts such as thin film dynamics, flame

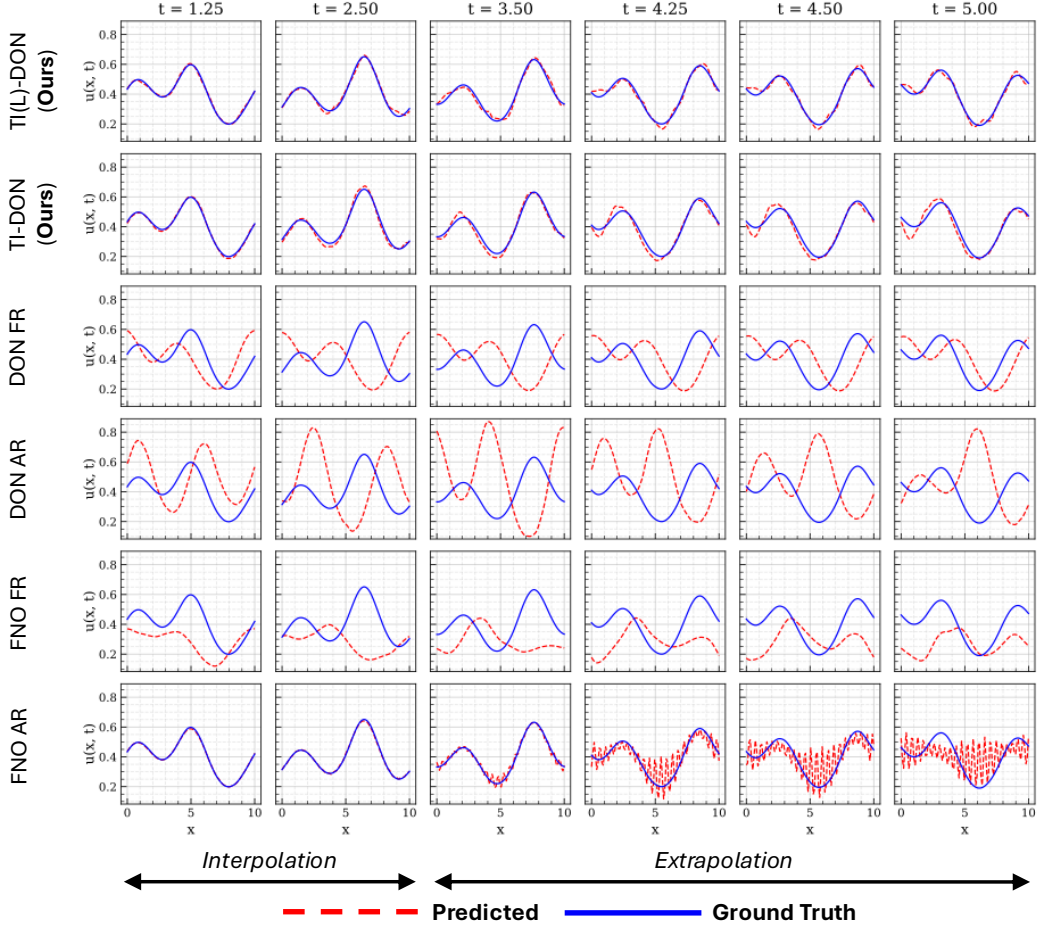


Figure 5: 1D KdV equation: Performance of all the frameworks in the training ($t \in [0, 2.5]$) and the extrapolation regime ($t \in [2.5, 5]$) for a representative sample.

fronts, reaction-diffusion systems, and plasma instabilities. The equation introduces a combination of nonlinear advection, second-order dissipation, and fourth-order dispersion terms, expressed as:

$$\frac{\partial u}{\partial t} = -u \frac{\partial u}{\partial x} - \frac{\partial^2 u}{\partial x^2} - \frac{\partial^4 u}{\partial x^4}, \quad (x, t) \in [0, L] \times (0, \infty) \quad (7)$$

$$u(x, t = 0) = u_0 \quad x \in [0, L] \quad (8)$$

Here, u represents the evolving scalar field with an initial profile u_0 . The spatial domain L is equipped with periodic boundary conditions. The nonlinear term $-u \frac{\partial u}{\partial x}$ accounts for advection,

while the dissipative term $\frac{\partial^2 u}{\partial x^2}$ contributes to numerical stability, and the high-order dispersive term $\frac{\partial^4 u}{\partial x^4}$ models the long-wavelength instability mechanisms that ultimately lead to chaotic dynamics. Further details regarding the data generation process are provided in SI C.3, where we adapt the data generation code from [16].

Figure 6 presents the prediction errors incurred by the time-integrator-based neural operators compared to standard baselines, shown for both the training and extrapolation temporal domains for a representative sample. In the training regime, DON FR and FNO AR accurately recover the solution profile, whereas DON AR and FNO FR exhibit relatively higher errors. However, in the extrapolation domain, several interesting behaviors emerge for the standard NO baselines. DON FR, DON AR, and FNO FR incur substantial errors once predictions extend beyond the training horizon, with these errors

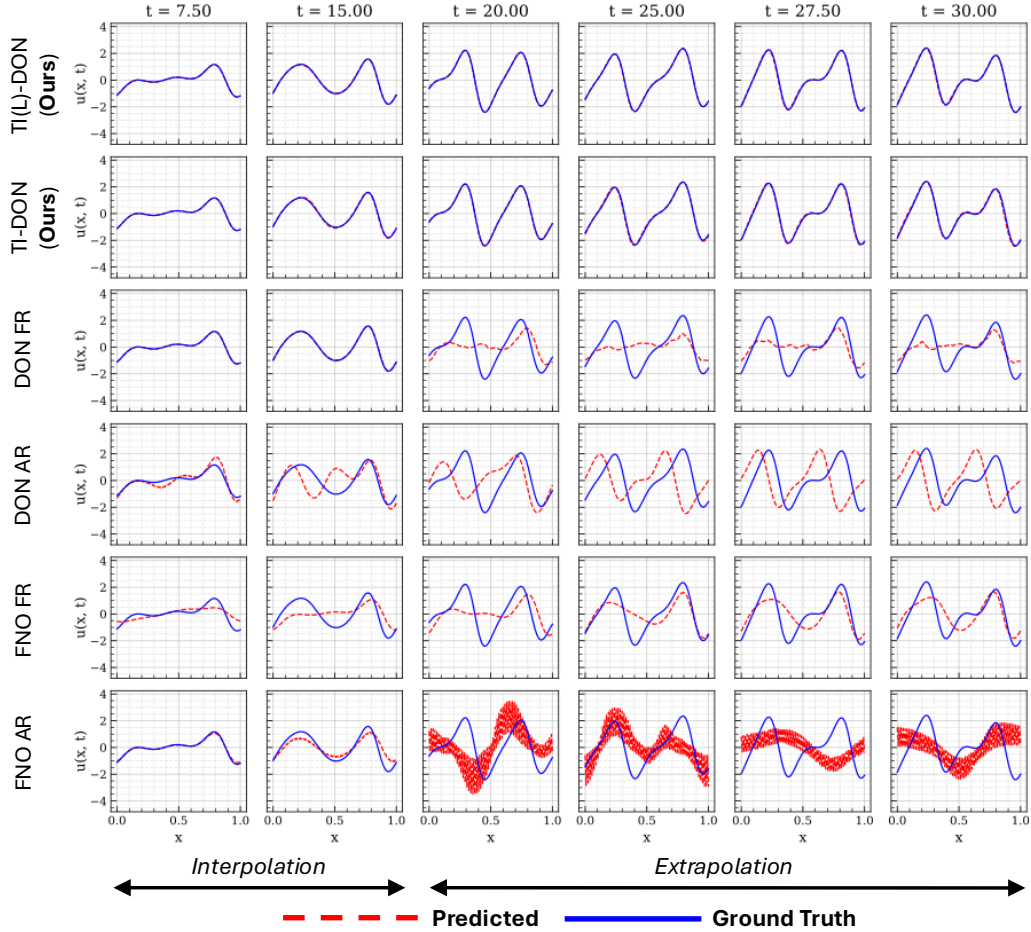


Figure 6: 1D KS equation: Performance of all the frameworks in the training ($t \in [0, 15]$) and the extrapolation regime ($t \in [15, 30]$) for a representative sample.

growing progressively as extrapolation time increases. Notably, FNO AR produces highly noisy and fluctuating solution profiles, indicative of spectral instability or spectral bias artifacts. This behavior manifests as high-frequency leakage, where certain unresolved or weakly controlled high-frequency modes become excessively amplified, resulting in pronounced oscillations in the predicted solution. This phenomenon closely resembles the instability observed in FNO AR predictions for the 1D KdV system. Interestingly, while such behavior was observed only for the KdV (dispersive) and KS (chaotic) systems but not for Burgers (dissipative), we also found that the training of FNO AR was inherently unstable for certain random weight initializations. This suggests that systems exhibiting dynamics beyond standard diffusion may not be well-suited for the FNO autoregressive learning paradigm. In contrast, the TI-based variants demonstrate remarkably higher predictive accuracy in both the training and extrapolation temporal domains. Once again, TI(L)-DeepONet performs slightly better in capturing the unseen chaotic dynamics of the KS equation, which can be attributed to its solution-specific local adaptivity during the learning process.

Figures 3(e) and (f) show the relative L_2 error growth over time for all frameworks. The autoregressive models, DON AR and FNO AR, are highly susceptible to error compounding under recursive rollout. Consequently, they begin accumulating errors within the initial timesteps, with these errors escalating rapidly in the extrapolation domain to reach values as high as 140% at the final timestep. FNO FR performs marginally better: while it still exhibits monotonically increasing error, the overall magnitude remains slightly lower, though still substantial in absolute terms. DON FR performs well in the training region due to DeepONet’s strong interpolation capabilities; however, its accuracy deteriorates rapidly upon entering the extrapolation domain, where errors grow steeply to reach levels

comparable to FNO FR (approximately 80% at the final timestep). In stark contrast, the proposed TI-based variants leverage learned system dynamics by incorporating numerical time integrators within the learning framework. This coupling effectively suppresses error growth in the extrapolation region, even in the presence of chaotic dynamics. Consequently, these models not only achieve high accuracy in the training domain but also maintain relatively stable and controlled error growth throughout the extrapolation interval $t \in [15, 30]$.

3.4 Two-dimensional Inviscid Burgers’ Equation

To assess performance on complex high-dimensional spatiotemporal dynamics, we consider the 2D Burgers’ equation, defined as:

$$\frac{\partial u}{\partial t} + u \frac{\partial u}{\partial x} + u \frac{\partial u}{\partial y} = \nu \left(\frac{\partial^2 u}{\partial x^2} + \frac{\partial^2 u}{\partial y^2} \right), \quad \forall (x, y, t) \in [0, 1]^2 \times [0, 1], \quad (9)$$

where $u(x, y, t)$ is a scalar field and $\nu = 10^{-4}$ is the kinematic viscosity. The initial condition, $u(x, y, 0) = s(x, y)$, is sampled from 2D Gaussian random fields, with periodic boundary conditions applied in both spatial dimensions. Although the equation includes a finite viscosity term, its magnitude is sufficiently small ($\nu = 10^{-4}$) as a result of which the system effectively behaves as inviscid, with shock formation expected at longer temporal horizons. This rich dynamical behavior, characterized by the development of sharp discontinuities and complex shock wave interactions, makes this problem an attractive benchmark for evaluating the performance of neural operator surrogates. SI C.4 contains comprehensive details of our data generation approach, which builds upon the code developed by [17].

Figure 7 presents the spatial error plots in both training and extrapolation regimes, demonstrating that the time integrator models overall achieve higher accuracy than the baseline models. The solution plot for the same sample is presented in Figure A2. Figures 3(g) and (h) compare the relative L_2 error trends over the entire temporal domain. Notably, we reduced the training temporal domain to $t \in [0, 0.33]$ with the extrapolation domain spanning $t \in [0.33, 1.0]$, yielding the most challenging case in this work; all networks must perform $3\times$ extrapolation with no prior knowledge of shock formation at longer temporal horizons (no training data contained shocks for any framework). The autoregressive DeepONet rapidly accumulates error, exceeding 130% by the final time step. The full rollout DeepONet initially performs better, but its fixed-basis representation limits temporal generalization, with errors surpassing TI-DeepONet beyond $t = 0.5$. Regarding the FNO variants, FNO FR fails catastrophically in capturing global system frequencies due to insufficient solution information across all timesteps, yielding completely unstable solution fields at longer temporal horizons with errors reaching 226% at the final timestep. FNO AR performs significantly better than DON AR, DON FR, and FNO FR, even outperforming the TI-based variants within the training temporal domain. However, due to its inherent sensitivity to error compounding during autoregressive inference, its excellent training domain accuracy (as low as 8% error) rapidly degrades in the extrapolation regime, reaching over 72% error at the final timestep, surpassing DON FR, which saturates at 52%. Consistent with previous examples, TI(L)-DeepONet maintains relatively slower and stable error growth, achieving final errors around 32% and outperforming all baselines as well as TI-DeepONet in the long-term prediction regime. These results demonstrate the robustness of time-integrator frameworks in modeling complex spatiotemporal stiff dynamics.

4 Choice of Inference Timestep

In our primary evaluations, TI-DeepONet was trained and tested using the same temporal resolution, i.e., the training and inference timesteps (Δt) were matched. However, the architecture’s compatibility with higher-order numerical integrators suggests that, in principle, inference may be conducted using timesteps different from those used during training. As long as the chosen Δt satisfies the Courant–Friedrichs–Lewy (CFL) stability condition, the resulting time integration should remain stable. This flexibility stems from the fact that TI-DeepONet mirrors traditional numerical solvers: both employ explicit time-stepping schemes, with TI-DeepONet approximating the right-hand side of the PDE via a neural operator rather than finite-difference or finite-element discretizations of spatial derivatives.

To investigate this capability, we performed preliminary experiments on the 1D Burgers equation, evaluating TI-DeepONet at three inference timesteps, $\Delta t \in 0.1, 0.01, 0.001$, while training was

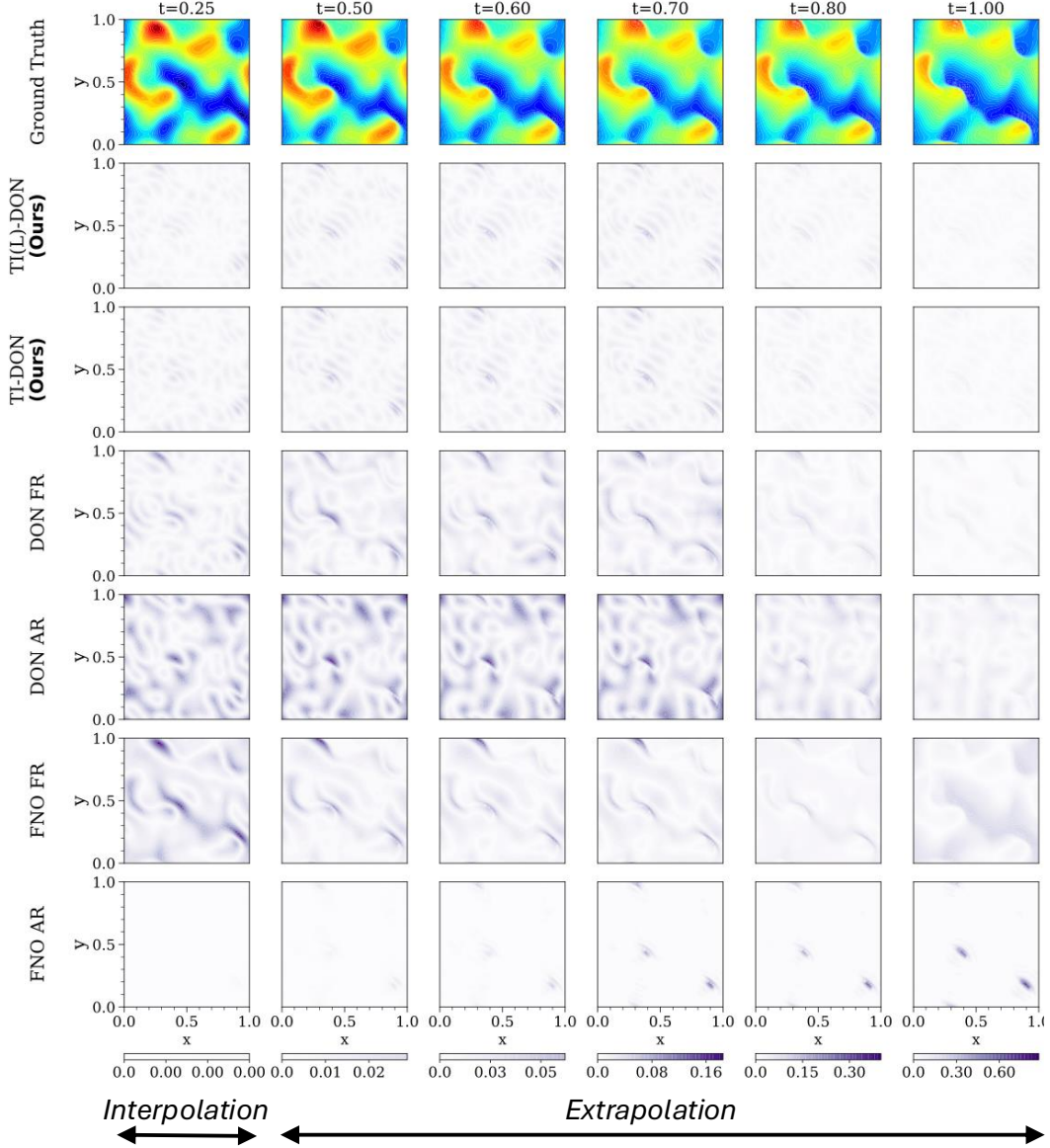


Figure 7: 2D Inviscid Burgers’ equation: Spatial error distribution across training ($t \in [0, 0.33]$) and extrapolation ($t \in [0.33, 1]$) regimes for all frameworks, illustrated with a representative sample.

performed at $\Delta t = 0.01$. Notably, TI-DeepONet preserved comparable L_2 error even when evaluated with a significantly coarser timestep ($\Delta t = 0.1$) than that used during training. This finding suggests the potential for developing more efficient surrogates that accelerate inference without additional training costs.

5 Conclusions

Accurate long-term extrapolation of dynamical systems remains a fundamental challenge for neural operators, particularly due to error accumulation in autoregressive predictions. To address this, we introduce TI-DeepONet and its adaptive variant TI(L)-DeepONet, which integrates classical numerical time integration with an operator learning framework (DeepONet). By reformulating the learning objective to approximate instantaneous time derivatives-subsequently integrated via high-order numerical schemes, our frameworks preserve the causal structure of dynamical systems while enhancing stability and accuracy in long-term forecasting. Furthermore, the operator learning

paradigm enables continuous spatiotemporal solutions for parametrized initial conditions, thereby enabling the construction of an efficient and reliable emulator for complex systems. Extensive evaluations across four canonical PDEs (1D/2D Burgers’, 1D KdV, and 1D KS equations) demonstrate the superiority of our approach. TI-DeepONet reduces relative L_2 extrapolation errors by 81% compared to autoregressive DeepONet and 70% compared to full-rollout methods, while maintaining stable predictions for temporal domains extending up to twice the training interval. The learnable coefficients in TI(L)-DeepONet further refine accuracy by adaptively weighting intermediate integration slopes, enabling solution-specific adjustments that outperform static numerical schemes in all our examples. By embedding temporal causality into the learning process and decoupling training-time integrators (e.g., Runge-Kutta) from inference-time integrators (e.g., Runge-Kutta or Adams-Bashforth), our methodology bridges neural operator flexibility with the robustness of numerical analysis. Among the proposed variants, TI(L)-DeepONet achieves the highest accuracy, albeit with a higher per-iteration computational cost due to its learnable integration coefficients (see SI Section A). However, this increase is offset by its significantly faster convergence to lower training loss, resulting in no net increase in total compute time. This hybrid paradigm offers a reliable pathway for modeling high-dimensional, time-dependent systems, where stability and generalizability are critical.

6 Limitations and Future Work

While our proposed frameworks demonstrate superior extrapolation accuracy compared to existing neural operator training strategies, they incur higher computational costs during both training and inference, as detailed in the SI Section A. Although these offline training costs can be justified by the consistent reliability of predictions across a wide range of parametric initial conditions, improving computational efficiency remains a key priority. To this end, we plan to leverage multi-GPU training and investigate methods for more efficient forward and backward propagation through the ODE solver. Additionally, we aim to extend the framework’s scalability to 3D and multiphysics systems and to incorporate adaptive time-stepping strategies for handling stiff dynamical systems.

Acknowledgments

The authors’ research efforts were partly supported by the National Science Foundation (NSF) under Grant No. 2438193 and 2436738. The authors would like to acknowledge computing support provided by the Advanced Research Computing at Hopkins (ARCH) core facility at Johns Hopkins University and the Rockfish cluster. ARCH core facility (`rockfish.jhu.edu`) is supported by the NSF grant number OAC1920103. The authors would also like to acknowledge Rajyasri Roy, who investigated the flexibility of the TI-DeepONet architecture and analyzed the inference accuracy when using coarser timesteps at inference compared to the finer timesteps used during training for the 1D Burgers equation. Any opinions, findings, conclusions, or recommendations expressed in this material are those of the author(s) and do not necessarily reflect the views of the funding organizations.

References

- [1] Lu Lu, Pengzhan Jin, Guofei Pang, Zhongqiang Zhang, and George Em Karniadakis. Learning nonlinear operators via DeepONet based on the universal approximation theorem of operators. *Nature machine intelligence*, 3(3):218–229, 2021.
- [2] Zongyi Li, Nikola Borislavov Kovachki, Kamyar Azizzadenesheli, Kaushik Bhattacharya, Andrew Stuart, Anima Anandkumar, et al. Fourier Neural Operator for Parametric Partial Differential Equations. In *International Conference on Learning Representations*.
- [3] Guang Lin, Christian Moya, and Zecheng Zhang. Learning the dynamical response of nonlinear non-autonomous dynamical systems with deep operator neural networks. *Engineering Applications of Artificial Intelligence*, 125:106689, 2023.
- [4] Sifan Wang and Paris Perdikaris. Long-time integration of parametric evolution equations with physics-informed DeepONets. *Journal of Computational Physics*, 475:111855, 2023.
- [5] Wuzhe Xu, Yulong Lu, and Li Wang. Transfer Learning Enhanced DeepONet for Long-Time Prediction of Evolution Equations. In *Proceedings of the AAAI Conference on Artificial Intelligence*, volume 37, pages 10629–10636, 2023.

- [6] W Diab and M Al Kobaisi. Temporal extrapolation and reliable generalization via 2u-nets deep operator network (2u-deeponet) for time-dependent pdes. In *ECMOR 2024*, volume 2024, pages 1–16. European Association of Geoscientists & Engineers, 2024.
- [7] Lizuo Liu and Wei Cai. Deeppropnet—a recursive deep propagator neural network for learning evolution pde operators. *arXiv preprint arXiv:2202.13429*, 2022.
- [8] Waleed Diab and Mohammed Al-Kobaisi. Temporal Neural Operator for Modeling Time-Dependent Physical Phenomena. *arXiv preprint arXiv:2504.20249*, 2025.
- [9] Katarzyna Michałowska, Somdatta Goswami, George Em Karniadakis, and Signe Riemer-Sørensen. Neural operator learning for long-time integration in dynamical systems with recurrent neural networks. In *2024 International Joint Conference on Neural Networks (IJCNN)*, pages 1–8. IEEE, 2024.
- [10] Ricardo Buitrago, Tanya Marwah, Albert Gu, and Andrej Risteski. On the Benefits of Memory for Modeling Time-Dependent PDEs. In *The Thirteenth International Conference on Learning Representations*.
- [11] Junyan He, Shashank Kushwaha, Jaewan Park, Seid Koric, Diab Abueidda, and Iwona Jasiuk. Sequential deep operator networks (S-DeepONet) for predicting full-field solutions under time-dependent loads. *Engineering Applications of Artificial Intelligence*, 127:107258, 2024.
- [12] Zheyuan Hu, Qianying Cao, Kenji Kawaguchi, and George Em Karniadakis. DeepOMamba: State-Space Model for Spatio-Temporal PDE Neural Operator Learning. *Available at SSRN 5149007*.
- [13] Ricky TQ Chen, Yulia Rubanova, Jesse Bettencourt, and David K Duvenaud. Neural ordinary differential equations. *Advances in neural information processing systems*, 31, 2018.
- [14] Tianping Chen and Hong Chen. Universal approximation to nonlinear operators by neural networks with arbitrary activation functions and its application to dynamical systems. *IEEE transactions on neural networks*, 6(4):911–917, 1995.
- [15] Samuel Lanthaler, Siddhartha Mishra, and George E Karniadakis. Error estimates for DeepONets: a deep learning framework in infinite dimensions. *Transactions of Mathematics and Its Applications*, 6(1):tnac001, 2022.
- [16] Zongyi Li, Miguel Liu-Schiaffini, Nikola Kovachki, Burigede Liu, Kamyar Azizzadenesheli, Kaushik Bhattacharya, Andrew Stuart, and Anima Anandkumar. Learning dissipative dynamics in chaotic systems. *arXiv preprint arXiv:2106.06898*, 2021.
- [17] Shawn G Rosofsky, Hani Al Majed, and EA Huerta. Applications of physics informed neural operators. *Machine Learning: Science and Technology*, 4(2):025022, 2023.

A Limitations: Computational costs

The improved extrapolation accuracy offered by the proposed TI-DeepONet and TI(L)-DeepONet approaches comes at the cost of increased training and inference times. This additional computational overhead stems from the repeated forward and backward passes through the time integrator. However, the convergence of TI-based networks is significantly faster, indicating more efficient optimization of network parameters compared to baseline methods. Table A1 presents a detailed comparison of the training and inference costs for each method across all benchmark problems. Moreover, incorporating adaptive, learnable slope coefficients facilitates convergence to the true solution even faster due to the solution-specific local adaptivity within the time integrator. Training and inference for the 1D Burgers’, 1D KdV, and 1D KS cases were conducted on a single NVIDIA A100 GPU equipped with 40GB memory (Intel Xeon Gold Cascade Lake). The 2D Burgers’ case was performed on a NVIDIA A100 GPU with 80GB memory (Intel Xeon Gold Icy Lake).

Table A1: Computational costs of training and inference for all examples across different frameworks.

Problem	Method	Batch size	Training time (iter/sec)	N_{test}	Inference time (sec)
Burgers’ (1D)	TI(L)-DON (Ours)	256	163.62	2500	5.48
	TI-DON AB (Ours)		195.43		5.86
	DON Full rollout		283.94		0.38
	DON Autoregressive		296.09		6.61
	FNO Full rollout		24.11		3.36
	FNO Autoregressive		285.32		2.12
KdV (1D)	TI(L)-DON (Ours)	256	179.82	1000	4.61
	TI-DON AB (Ours)		208.59		4.47
	DON Full rollout		234.98		1.22
	DON Autoregressive		298.44		5.98
	FNO Full rollout		10.96		6.31
	FNO Autoregressive		306.53		1.49
KS (1D)	TI(L)-DON (Ours)	128	117.55	3000	7.67
	TI-DON AB (Ours)		122.11		8.12
	DON Full rollout		22.39		5.26
	DON Autoregressive		232.62		7.15
	FNO Full rollout		4.52		7.16
	FNO Autoregressive		341.34		5.13
Inviscid Burgers’ (2D)	TI(L)-DON (Ours)	32	8.91	1000	8.57
	TI-DON AB (Ours)		9.85		4.56
	DON Full rollout		64.23		2.29
	DON Autoregressive		37.71		8.26
	FNO Full rollout		2.67		19.85
	FNO Autoregressive		97.96		13.66

Training cost analysis: During training, the computational complexity varies across methods. The branch network requires $\mathcal{O}(bs)$ forward passes per iteration, where bs represents the batch size. The trunk network evaluation complexity depends on the strategy employed:

- Full rollout: $\mathcal{O}(n_s \times n_t)$ forward passes, where n_s is the number of spatial points and n_t is the number of temporal locations.
- Autoregressive methods (autoregressive DeepONet, TI-DeepONet, and TI(L)-DeepONet): $\mathcal{O}(n_s)$ forward passes because of the absence of temporal dimension.

For TI(L)-DeepONet, an additional $\mathcal{O}(bs)$ forward passes are required per iteration to evaluate the auxiliary deep neural network that learns the intermediate RK4 slopes. As a result, TI(L)-DeepONet incurs the highest per-iteration cost, leading to the lowest iteration speed observed in Table A1.

Although TI-DeepONet and autoregressive DeepONet evaluate a similar number of forward passes, TI-DeepONet additionally invokes the time integrator, introducing extra forward computations. Consequently, it is more expensive to train than autoregressive DeepONet but still cheaper than TI(L)-DeepONet. The cost of the full rollout method scales directly with the spatiotemporal resolution. While it avoids recursion, the simultaneous prediction over all space-time points makes it more expensive than autoregressive methods, which predicts for only spatial points at each step. The trends observed in Table A1 align with this analysis. Note that in the 2D Burgers’ case, the relatively higher training cost incurred by the autoregressive DeepONet is due to the use of additional hidden layers in the trunk network.

Inference cost analysis: During inference, full rollout is the fastest method, requiring $\mathcal{O}(N_{\text{test}}) + \mathcal{O}(n_s \times n_t)$ forward passes for total evaluation, where N_{test} is the number of test samples. In contrast, the autoregressive, TI-DeepONet, and TI(L)-DeepONet methods perform recursive time predictions, resulting in longer inference times. For evaluating N_{test} samples, the autoregressive networks simulate $n_t \times \mathcal{O}(N_{\text{test}}) + n_t \times \mathcal{O}(n_s)$ forward passes. During inference, the additional network in the TI(L)-DeepONet is not evaluated as the optimized parameters are already obtained, resulting in no additional cost.

B Statistical Variability

To evaluate the performance of the model, we compute the relative L_2 error of the extrapolation predictions, and report the mean and standard deviation of this metric based on five independent training trials in Table A2.

Across five independent trial runs, TI(L)-DeepONet consistently achieves the lowest extrapolation error across all benchmark problems. In addition to superior accuracy, it also exhibits reduced variance in error estimates, indicating enhanced robustness and reliability. As expected, both the full rollout and autoregressive DeepONet models suffer from substantially higher errors, particularly outside the training temporal domain. Similarly, the FNO variants, both full rollout and autoregressive incur higher errors. FNO FR generally exhibits higher errors throughout the entire temporal domain and yields particularly unstable solutions due to its inability to capture all global frequencies of the system. Notably, this limitation also manifests as higher variance in the predictions. For FNO AR, spectral instability causes error spikes in the extrapolation domain, leading to higher solution variance - consistent with our observations highlighted in Sec. 3. Overall, the TI-based frameworks not only enhance extrapolation accuracy but also offer greater robustness across random initializations, underscoring their effectiveness for modeling time-dependent PDEs.

C Additional details

C.1 One-dimensional Burgers’ Equation

Data generation: The initial condition $s(x)$ is sampled from a Gaussian random field with spectral density $S(k) = \sigma^2(\tau^2 + (2\pi k)^2)^{-\gamma}$, where $\sigma = 25$, $\tau = 5$, and $\gamma = 4$. This ensures $s(x)$ is periodic on $x \in [0, 1]$. The corresponding kernel is expressed via inverse Fourier transform as $K(\mathbf{x}, \mathbf{x}') = \int_{-\infty}^{\infty} S(k)e^{2\pi i k(\mathbf{x}-\mathbf{x}')} dk$. We discretize the spatiotemporal domain using 101 grid points along each dimension.

Data preparation: The training and testing datasets are constructed differently depending on the learning strategy employed. In the full rollout setting, the goal is to train a DeepONet/FNO to learn a solution operator \mathcal{G}_θ that maps an initial condition $s(x)$ to the full spatiotemporal solution $u(x, t)$. For this purpose, we consider a set of initial conditions, spatiotemporal query locations, and the corresponding solution fields. The data is partitioned into training and testing sets using a train-test split ratio of 0.8, yielding $N_{\text{train}} = 2000$ and $N_{\text{test}} = 500$ samples. Importantly, we aim to assess the performance of various frameworks in learning the full spatiotemporal field over the entire temporal domain when given access to solutions at limited timesteps. To this end, we restrict training to only half of the temporal domain, i.e., $t_{\text{train}} \in [0, 0.5]$. Consequently, the grid for the trunk network is formed by taking a meshgrid over spatiotemporal coordinates (x, t) , where $x \in [0, 1]$ and $t \in [0, 0.5]$

Table A2: Relative L_2 errors reported based on five independent training trials for all frameworks in the extrapolation regime.

Problem	Method	Relative L_2 error			
		$t+10\Delta t_e$	$t+20\Delta t_e$	$t+40\Delta t_e$	T^*
Burgers' (1D)	TI(L)-DON	0.019±0.003	0.023±0.003	0.036±0.004	0.044±0.005
	TI-DON AB	<u>0.031±0.004</u>	<u>0.037±0.005</u>	<u>0.057±0.008</u>	<u>0.070±0.011</u>
	DON FR	0.043±0.002	0.095±0.004	0.247±0.028	0.336±0.053
	DON AR	0.710±0.089	1.004±0.144	1.556±0.206	1.768±0.227
	FNO FR	0.219±0.026	0.243±0.025	0.291±0.019	0.456±0.147
	FNO AR	0.202±0.041	0.212±0.048	0.215±0.059	0.216±0.062
KdV (1D)	TI(L)-DON	0.054±0.019	0.065±0.027	0.075±0.031	0.111±0.051
	TI-DON AB	<u>0.086±0.026</u>	<u>0.108±0.034</u>	<u>0.129±0.043</u>	<u>0.183±0.063</u>
	DON FR	0.776±0.0004	0.716±0.0005	0.719±0.0005	0.795±0.0007
	DON AR	0.823±0.073	0.886±0.064	0.922±0.069	0.968±0.083
	FNO FR	0.900±0.038	0.828±0.027	0.756±0.025	0.681±0.033
	FNO AR	0.343±0.086	0.443±0.096	0.496±0.091	0.543±0.095
KS (1D)	TI(L)-DON	0.048±0.006	0.088±0.009	0.230±0.016	0.331±0.018
	TI-DON AB	<u>0.058±0.010</u>	<u>0.103±0.016</u>	<u>0.248±0.018</u>	<u>0.349±0.017</u>
	DON FR	0.598±0.130	0.924±0.019	0.844±0.003	0.885±0.028
	DON AR	1.199±0.056	1.218±0.048	1.264±0.046	1.294±0.045
	FNO FR	0.921±0.002	0.946±0.004	0.889±0.004	0.922±0.008
	FNO AR	1.596±0.260	1.668±0.271	1.744±0.278	1.765±0.303
Inviscid Burgers' (2D)	TI(L)-DON	<u>0.186±0.003</u>	<u>0.223±0.004</u>	0.292±0.005	0.324±0.005
	TI-DON AB	0.189±0.002	0.226±0.003	<u>0.297±0.003</u>	<u>0.330±0.003</u>
	DON FR	0.373±0.042	0.412±0.032	0.494±0.028	0.534±0.039
	DON AR	0.883±0.275	1.089±0.364	1.532±0.553	1.765±0.661
	FNO FR	0.315±0.023	0.345±0.027	0.742±0.597	1.689±0.764
	FNO AR	0.096±0.013	0.208±0.051	0.767±0.432	1.37±1.004

during training, while $t \in [0, 1]$ during testing. This same meshgrid is also employed for computing the 2D Fourier Transform in FNO full rollout.

For training the autoregressive DeepONet, autoregressive FNO, TI-DeepONet, and TI(L)-DeepONet architectures, we adopt a different strategy for preparing the training and testing datasets. In autoregressive methods, future states of the system are recursively predicted using the model's own previous outputs as inputs at each timestep. This approach inherently leads to error accumulation, as prediction errors at one timestep propagate and potentially amplify at subsequent timesteps. Understanding and mitigating this issue is a key motivation behind the TI-DeepONet architecture. To this end, the training dataset is created as follows: the input to the branch network consists of stacked solution states from $t = 0$ to $t = 0.5$, i.e., $[u^0(x), u^1(x), \dots, u^{50}(x)]$. Similarly, the output ground truth consists of stacked solution states from $t = 0.01$ to $t = 0.51$, i.e., $[u^1(x), u^2(x), \dots, u^{51}(x)]$. This arrangement enables the solution operator \mathcal{G}_θ to learn the mapping $u^i(x) \rightarrow u^{i+1}(x)$, where $u^i(x)$ and $u^{i+1}(x)$ represent the solution states at the i^{th} and $(i+1)^{\text{th}}$ timesteps, respectively. The trunk network processes only the spatial coordinates $x \in [0, 1]$. For autoregressive FNO, the inputs and outputs are distinct $u^i(x)$ and $u^{i+1}(x)$ solution pairs, and the Fourier transform is one-dimensional and is applied only in the x -dimension.

Training architecture: Tables A3 and A4 present the network architecture details, including the number of layers and neurons per layer, activation functions, total epochs to convergence, batch size, and Fourier modes (where applicable). For the TI(L)-DeepONet architecture, we additionally

employ an auxiliary feedforward network designed to predict the four RK4 slope coefficients. This network consists of two hidden layers with 32 neurons each, followed by an output layer with four neurons. The hidden layers use the `tanh` activation function, while a `softmax` activation is applied at the output layer to ensure the predicted coefficients sum to one. Training was performed using the Adam optimizer with an initial learning rate of 10^{-3} , which was exponentially decayed by a factor of 0.95 every 5000 epochs. A similar learning rate scheduling strategy was employed for the auxiliary network predicting the adaptive RK4 slope coefficients. Notably for FNO AR, the learning rate schedule also employed exponential decay but by a factor of 0.96 every 2000 steps. Both training and test losses were monitored at each epoch. The final model corresponds to the set of parameters that yielded the lowest test loss over the entire training process. Among all tested architectures, TI(L)-DeepONet exhibited the fastest convergence, attributed to its capacity to adapt to the local dynamics of the solution. Later in this section, we examine the evolution of the learned RK4 slope coefficients across epochs and compare them to the reference coefficients: $\frac{1}{6}, \frac{2}{6}, \frac{2}{6}, \frac{1}{6}$.

Table A3: 1D Burgers' equation: Neural network architecture and training settings across different DeepONet-based methods.

Method	Branch Net	Trunk Net	Activation	Epochs	Batch Size
TI(L)-DON	[101], [100]×6, [60]	[100]×6, [60]	Tanh	1×10^5	256
TI-DON	[101], [100]×6, [60]	[100]×6, [60]	Tanh	1×10^5	256
DON FR	[128]×6, [60]	[128]×6, [60]	Tanh	2×10^5	256
DON AR	[101], [100]×6, [60]	[100]×6, [60]	Tanh	1×10^5	256

Table A4: 1D Burgers' equation: Neural network architecture and training settings across different FNO-based methods.

Method	Fourier Blocks	Modes	Hidden Dim	Activation	Epochs	Batch Size
FNO AR	6	24	64	GELU	30000	128
FNO FR	4	16	32	GELU	5000	64

Learnable Weights: As previously discussed, the learnable slope coefficients $\alpha = [\alpha_1, \alpha_2, \alpha_3, \alpha_4]$ are predicted by the additional NN, which takes the current solution state u^i as input, i.e., $\alpha = \text{NN}_\theta(u^i)$. Analyzing the evolution of these solution-specific coefficients over training epochs provides insight into how the network adapts the time integrator to local dynamics, in contrast to using a fixed set of RK4 coefficients. This comparison is illustrated in Fig. A1. The dashed blue line in each plot indicates the reference slope coefficients typically used in the RK4 method, derived from a Taylor series expansion. These coefficients result in a fourth-order accurate scheme and are generally expected to provide high accuracy for traditional time integrators. However, in the context of the operator learning framework, these coefficients also adapt to the approximation error of the neural operator. Making these slope coefficients learnable allows the model to better compensate for such errors, thereby improving the overall accuracy of the framework.

C.2 One-dimensional Korteweg-de Vries (KdV) Equation

Data generation: The initial condition, $u(x, 0)$ is defined as a sum of two solitons, i.e., $u = u_1 + u_2$. A soliton is a nonlinear, self-reinforcing, localized wave packet that is strongly stable. It is expressed as:

$$u_i(x, 0) = 2k_i^2 \text{sech}^2 \left(k_i \left(\left(x + \frac{P}{2} - Pd_i \right) \% P - \frac{P}{2} \right) \right)^2 \quad (10)$$

where sech is hyperbolic secant, P is the period in space, $\%$ is the modulo operator, $i = \{1, 2\}$, $k \in [0.5, 1]$ and $d \in [0, 1]$ are the coefficients that determine the height and location of the soliton peak, respectively. The dataset is curated by generating $N = 1000$ distinct initial conditions and their temporal evolution is modeled using the midpoint method. The 1D spatial domain, $\Omega = [0, 10]$, is discretized into 100 uniformly spaced grid points, resulting in a spatial resolution of $\Delta x = 0.1$. For

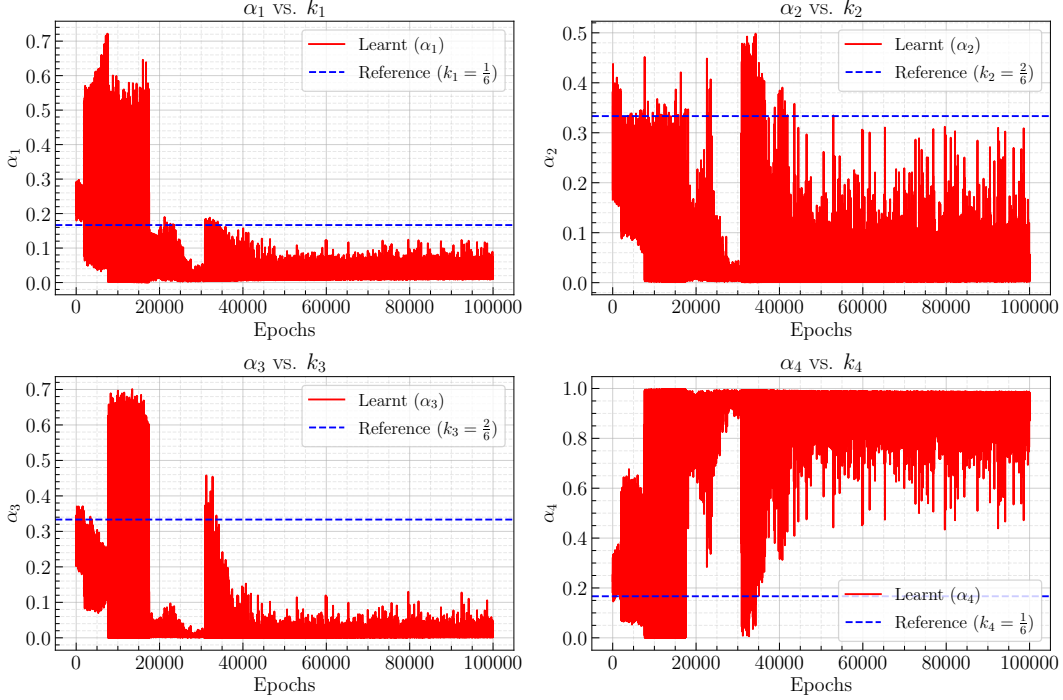


Figure A1: 1D Burgers’ Equation: Epoch-wise change of the learnable RK4 slope coefficients $\alpha = [\alpha_1, \alpha_2, \alpha_3, \alpha_4]$.

the temporal domain, we consider a uniform grid of 201 points spanning the time domain $t \in [0, 5]$, which yields a $\Delta t = 0.025$.

Data preparation: To assess the extrapolation accuracy of the different methods, we train only on the first half of the temporal domain, i.e., $t_{\text{train}} \in [0, 2.5]$, and evaluate predictive performance over the entire domain ($t \in [0, 5]$). To reiterate, in the full rollout setting, the inputs to the trunk network are constructed from a meshgrid of (x, t_{train}) , whereas in the autoregressive setting, only the spatial coordinates (x) are used as trunk inputs. Similarly, the same meshgrid that serves as trunk inputs during DeepONet FR training becomes the axes along which the 2D Fourier transform is performed (all x coordinates, seen t coordinates) for FNO FR training. While the initial condition samples serve as input to the branch network in the DeepONet full rollout model, the input to the branch network in the autoregressive and TI-based DeepONet frameworks consists of stacked solution states from $t = 0$ to $t = 2.5$, i.e., $[u^0(x), u^1(x), \dots, u^{100}(x)]$. For autoregressive FNO, the inputs and outputs are the solution pairs $u^i(x)$ and $u^{i+1}(x)$, with the 1D Fourier transform applied along the spatial dimension x only. The train-test split is maintained at 0.8.

Training architecture: Tables A5 and A6 present the network architecture details, including the number of layers, neurons per layer, activation functions, total epochs to convergence, batch size, and Fourier modes (where applicable). For the TI(L)-DeepONet framework, we employ a secondary feedforward network to predict the four RK4 slope coefficients. This network consists of two hidden layers with 64 and 48 neurons, respectively, followed by an output layer with four neurons. The hidden layers use the `tanh` activation function, while a `softmax` activation is applied at the output layer to ensure that the predicted coefficients sum to one. Training was performed using the Adam optimizer with an initial learning rate of 10^{-3} , which was exponentially decayed by a factor of 0.95 every 5000 epochs. A similar learning rate schedule was used for training the auxiliary network tasked with learning the RK4 slope coefficients. The same learning rate schedule with identical hyperparameters was employed for FNO FR training. For FNO AR, an exponential decay learning rate schedule was also used, but with an initial learning rate of 10^{-3} that decayed by a factor of 0.96 every 2000 steps.

Table A5: 1D KdV equation: Neural network architecture and training settings across different DeepONet methods.

Method	Branch Net	Trunk Net	Activation	Epochs	Batch Size
TI(L)-DON	[128]×6, [80]	[128]×6, [80]	Tanh	1.5×10^5	256
TI-DON	[128]×6, [80]	[128]×6, [80]	Tanh	1×10^5	256
DON FR	[150, 250, 450, 380, 320, 300, 80]	[200, 220, 240, 250, 260, 280, 300, 80]	Swish	1×10^5	256
DON AR	[128]×6, [80]	[128]×6, [80]	Tanh	1×10^5	256

Table A6: 1D KdV equation: Neural network architecture and training settings across different FNO-based methods.

Method	Fourier Blocks	Modes	Hidden Dim	Activation	Epochs	Batch Size
FNO AR	6	24	64	GELU	30000	128
FNO FR	6	32	64	GELU	10000	64

C.3 One-dimensional Kuramoto-Sivashinsky (KS) Equation

Data generation: We consider the 1D Kuramoto-Sivashinsky (KS) equation on a spatial domain $x \in [0, L]$ with $L = 6\pi$, equipped with periodic boundary conditions. The initial conditions $u(x, 0) = s(x)$ are sampled from mean-zero Gaussian random fields (GRFs) with periodic boundary conditions. Specifically, we generate GRFs with covariance operator $C = \sigma^2(-\Delta + \tau^2 I)^{-\gamma}$, where $\gamma = 1$, $\tau = 2$, and $\sigma = 1$. The spatial domain is discretized using $N_x = 128$ grid points, and the temporal domain $t \in [0, 30]$ is discretized with $N_t = 300$ timesteps. The PDE is solved using the exponential time-differencing fourth-order Runge-Kutta (ETDRK4) method with a timestep of $\Delta t = 0.1$. We generate a total of 3000 samples, each consisting of the initial condition and the corresponding spatiotemporal solution field $u(x, t)$. The dataset is partitioned using a train-test split ratio of 0.8, yielding $N_{\text{train}} = 2400$ training samples and $N_{\text{test}} = 600$ testing samples. The periodic boundary conditions ensure that the solution remains in the space of mean-zero periodic functions throughout the evolution, preserving the chaotic dynamics characteristic of the KS equation.

Data preparation: For evaluating the extrapolation capabilities of various methods, we restrict training to the initial half of the temporal domain, specifically $t_{\text{train}} \in [0, 15]$, while testing spans the complete temporal interval $t \in [0, 30]$. In the full rollout configuration, the trunk network receives spatiotemporal coordinate pairs (x, t_{train}) arranged in a meshgrid format. Conversely, the autoregressive approach utilizes only spatial coordinates x as trunk inputs. For FNO FR, the 2D Fourier transform operates along both spatial and temporal dimensions using the same coordinate grid employed in DeepONet FR training. The branch network architecture differs between approaches: full rollout DeepONet processes initial conditions $s(x)$ directly, while autoregressive and TI-based variants receive a sequence of solution snapshots spanning $t = 0$ to $t = 15$, comprising states $[u^0(x), u^1(x), \dots, u^{150}(x)]$, with the corresponding output solution states $[u^1(x), u^2(x), \dots, u^{151}(x)]$. The autoregressive FNO framework also operates on consecutive solution pairs $(u^i(x), u^{i+1}(x))$ as input-output mappings, employing a 1D Fourier transform exclusively in the spatial dimension.

Training architecture: Tables A7 and A8 present the network architecture details, including the number of layers, neurons per layer, activation functions, total epochs to convergence, batch size, and Fourier modes (where applicable). All DeepONet variants employ Fourier feature encoding in the trunk network. For the full rollout DeepONet, both spatial and temporal coordinates (x, t) are augmented with sinusoidal features computed as $[\sin(\pi kx), \cos(\pi kx), \sin(\pi kt), \cos(\pi kt)]$ for $k \in \{1, 2, \dots, 10\}$, expanding the input dimension from 2 to 42. For the autoregressive and TI-based variants, only the spatial coordinate x is augmented with Fourier features $[\sin(\pi kx), \cos(\pi kx)]$, expanding the input dimension from 1 to 21. For the TI(L)-DeepONet framework, we employ an auxiliary feedforward network to predict the four RK4 slope coefficients. This network consists

of two hidden layers with 64 neurons each, followed by an output layer with four neurons. The hidden layers utilize the `tanh` activation function, while a `softmax` activation is applied at the output layer to ensure the predicted coefficients sum to one. All DeepONet variants (DON FR, DON AR, TI-DON, and TI(L)-DON) are trained using the AdamW optimizer with an initial learning rate of 10^{-3} , exponentially decayed by a factor of 0.95 every 5000 epochs, and a weight decay of 10^{-4} . For TI(L)-DeepONet specifically, the auxiliary RK4 network is trained separately using the Adam optimizer with an initial learning rate of 2×10^{-3} and the same exponential decay schedule. The FNO variants employ the Adam optimizer with an initial learning rate of 10^{-3} , exponentially decayed by a factor of 0.96 every 2000 steps for both FNO FR and FNO AR configurations.

Table A7: 1D KS equation: Neural network architecture and training settings across different DeepONet methods.

Method	Branch Net	Trunk Net	Activation	Epochs	Batch Size
TI(L)-DON	[128]×7, [100]	[128]×7, [100]	Branch: Tanh Trunk: Sine	1.75×10^5	128
TI-DON	[128]×7, [100]	[128]×7, [100]	Branch: Tanh Trunk: Sine	1.5×10^5	128
DON FR	[128]×7, [100]	[128]×7, [100]	Branch: SiLU Trunk: Sine	1.5×10^5	128
DON AR	[128]×7, [100]	[128]×7, [100]	Branch: Tanh Trunk: Sine	1.5×10^5	128

Table A8: 1D KS equation: Neural network architecture and training settings across different FNO-based methods.

Method	Fourier Blocks	Modes	Hidden Dim	Activation	Epochs	Batch Size
FNO AR	6	64	64	GELU	10000	64
FNO FR	6	64	64	GELU	7000	64

C.4 Two-dimensional Inviscid Burgers’ Equation

Data generation: For the 2D inviscid Burgers’ equation, we consider periodic boundary conditions on a unit square domain $(x, y) \in [0, 1]^2$. The initial conditions $u(x, y, 0) = s(x, y)$ are sampled from periodic Matérn-type Gaussian random fields with length scale $l = 0.1$ and standard deviation $\sigma = 0.2$. The spatial domain is discretized using a 32×32 grid with $N_x = N_y = 32$ points. The PDE is solved using a fourth-order Runge-Kutta scheme with timestep $\Delta t = 10^{-4}$ up to final time $t = 1.0$. Solutions are saved at intervals of $\Delta t_{\text{save}} = 0.01$, resulting in 101 temporal snapshots. The kinematic viscosity is set to $\nu = 10^{-4}$, which is sufficiently small to approximate inviscid behavior while maintaining numerical stability. We generate a total of 1000 samples, each consisting of the initial condition and the corresponding spatiotemporal solution field $u(x, y, t)$ of size $101 \times 64 \times 64$.

Data preparation: The dataset is partitioned using a train-test split ratio of 0.8, yielding $N_{\text{train}} = 800$ training samples and $N_{\text{test}} = 200$ testing samples. To evaluate extrapolation capabilities, we train only on the first third of the temporal domain, i.e., $t_{\text{train}} \in [0, 0.33]$ (33 out of 101 time steps), and assess performance over the entire domain $t \in [0, 1.0]$. This represents the most challenging extrapolation scenario in our study, requiring $3 \times$ temporal extrapolation with no exposure to shock formation during training.

For full rollout methods, our aim is to learn a solution operator \mathcal{G}_θ that maps initial conditions to the full solution: $u_0(x, y) \rightarrow u(t, x, y)$. The trunk network receives (x, y, t_{train}) coordinates as input, while the branch network processes the initial conditions. For FNO FR, the 3D Fourier transform is performed along all three dimensions (x, y, t_{train}) , capturing the full spatiotemporal frequency content within the training domain. In contrast, autoregressive and TI-based methods use only spatial coordinates (x, y) for the trunk network input. Their branch networks receive stacked solution

states $[u^0(x, y), u^1(x, y), \dots, u^{33}(x, y)]$ from the training temporal window. FNO AR employs a 2D Fourier transform along the spatial dimensions (x, y) only, consistent with its autoregressive nature to learn a one-step mapping between pairs of consecutive solution states $(u^i(x, y), u^{i+1}(x, y))$. Note that for the autoregressive/TI-based variants, explicit temporal information is absent and instead is assimilated in the batch dimension.

Training architecture Tables A9 and A10 presents the network architecture details, including the number of layers and neurons per layer, activation functions, total epochs to convergence, batch size and Fourier modes (if applicable). All DeepONet variants employ Fourier feature encoding in the trunk network. For the full rollout DeepONet, the spatial and temporal coordinates (x, y, t) are augmented with sinusoidal features computed as $[\sin(\pi kx), \cos(\pi kx), \sin(\pi ky), \cos(\pi ky), \sin(\pi kt), \cos(\pi kt)]$ for $k \in \{1, 2, \dots, 10\}$, expanding the input dimension from 3 to 63. For the autoregressive and TI-based variants, only the spatial coordinates (x, y) are augmented with Fourier features $[\sin(\pi kx), \cos(\pi kx), \sin(\pi ky), \cos(\pi ky)]$, expanding the input dimension from 2 to 42. In this case, for the TI(L)-DeepONet architecture, we employ a similar combination of 2D convolutional blocks and MLP layers as used in the branch network to learn the RK4 slope coefficients. The convolutional blocks utilize the same combination of Conv2D and pooling layers as the branch, with the only difference being that the Conv2D layers have a reduced number of filters (32 instead of 64). This is followed by a flattening layer, after which the intermediate representation is passed through two fully connected hidden layers and finally to an output layer with 4 neurons that predicts the RK4 slope coefficients.

The Conv2D layers use a ReLU activation function, the fully connected hidden layers use \tanh , and the output layer applies a softmax activation to ensure that the predicted slope coefficients sum to one. Training was performed using the Adam optimizer with an initial learning rate of 10^{-3} , which was exponentially decayed by a factor of 0.95 every 5000 steps. The auxiliary network responsible for predicting the learnable RK4 slope coefficients was trained with a similar exponential decay schedule, but with a higher initial learning rate of 2×10^{-3} . For both FNO AR and FNO FR variants, we employ a similar exponential decay schedule as the DeepONet variants albeit with a decay factor of 0.96 every 2000 steps.

Table A9: 2D Inviscid Burgers' equation: Neural network architecture and training settings across different methods.

Method	Branch Net	Trunk Net	Activation	Epochs	Batch Size
TI(L)-DON	Conv2D(features = 64, kernel size = (3,3), strides = 1), MaxPool(window shape=(2, 2), strides = (2, 2)), Conv2D(features = 64, kernel size = (3,3), strides = 1), MaxPool(window shape=(2, 2), strides = (2, 2)), Conv2D(features = 64, kernel size = (2,2), strides = 1), Avg-Pool(window shape = (2,2), strides = (2,2)), MLP([256, 128, 100])	[128]×6, [100]	(1) Branch: Conv2D - ReLU, MLP - GELU, (2) Trunk: WaveletAct	2.25×10^5	64

Continued on next page

Table A9 – Continued from previous page

Method	Branch Net	Trunk Net	Activation	Epochs	Batch Size
TI-DON	Conv2D(features = 64, kernel size = (3,3), strides = 1), MaxPool(window shape=(2, 2), strides = (2, 2)), Conv2D(features = 64, kernel size = (3,3), strides = 1), MaxPool(window shape=(2, 2), strides = (2, 2)), Conv2D(features = 64, kernel size = (2,2), strides = 1), Avg-Pool(window shape = (2,2), strides = (2,2)), MLP([256, 128, 100])	[128]×6, [100]	(1) Branch: Conv2D - ReLU, MLP - GELU, (2) Trunk: WaveletAct	2×10^5	64
DON FR	Conv2D(features = 64, kernel size = (3,3), strides = 1), MaxPool(window shape=(2, 2), strides = (2, 2)), Conv2D(features = 64, kernel size = (3,3), strides = 1), MaxPool(window shape=(2, 2), strides = (2, 2)), Conv2D(features = 64, kernel size = (2,2), strides = 1), Avg-Pool(window shape = (2,2), strides = (2,2)), MLP([256, 128, 100])	[128]×5, [100]	(1) Branch: Conv2D - GELU, MLP - GELU, (2) Trunk: WaveletAct	1×10^5	128
DON AR	Conv2D(features = 64, kernel size = (3,3), strides = 1), MaxPool(window shape=(2, 2), strides = (2, 2)), Conv2D(features = 64, kernel size = (3,3), strides = 1), MaxPool(window shape=(2, 2), strides = (2, 2)), Conv2D(features = 64, kernel size = (2,2), strides = 1), Avg-Pool(window shape = (2,2), strides = (2,2)), MLP([256, 128, 128, 100])	[128]×6, [100]	(1) Branch: Conv2D - ReLU, MLP - Tanh, (2) Trunk: Sine	2×10^5	64

Table A10: 2D Burgers' equation: Neural network architecture and training settings across different FNO-based methods.

Method	Fourier Blocks	Modes	Hidden Dim	Activation	Epochs	Batch Size
FNO AR	6	12	64	GELU	1000	128
FNO FR	6	12	64	GELU	5000	32

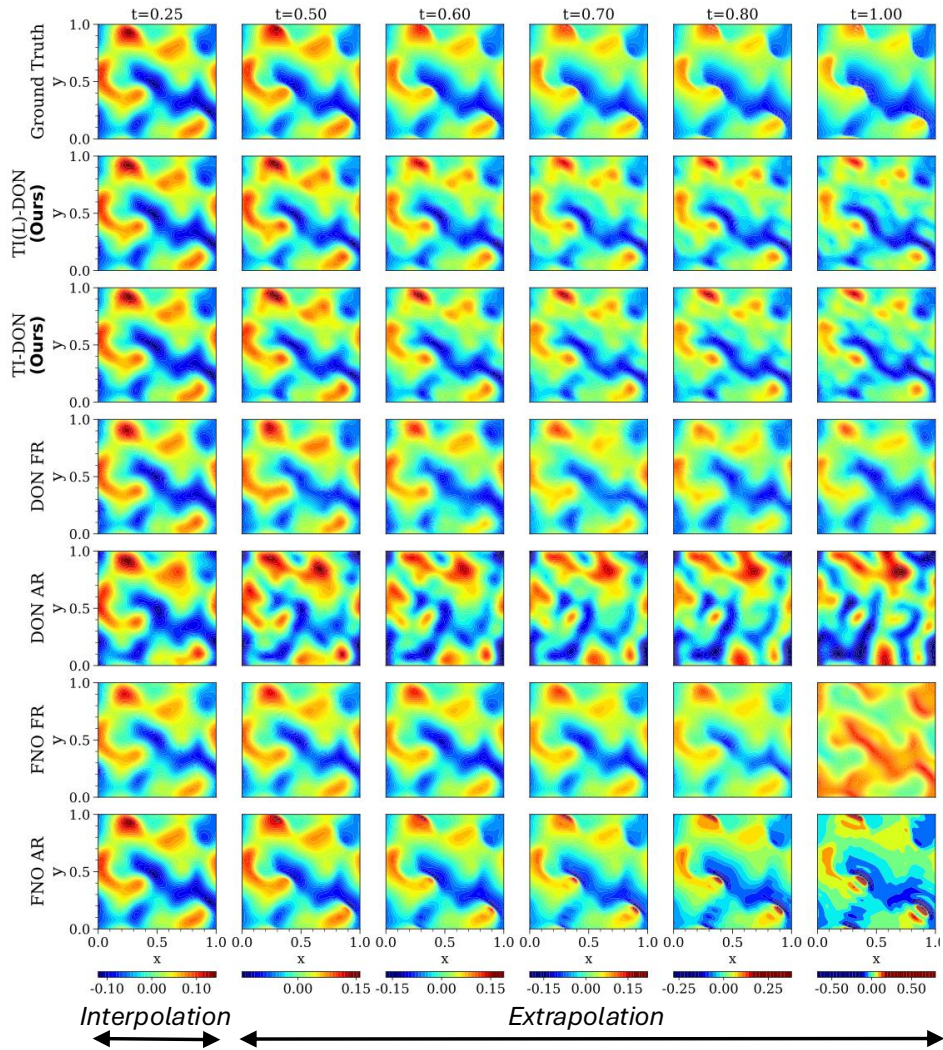


Figure A2: 2D Inviscid Burgers' equation: Solution field for a representative sample, shown across both the training regime ($t \in [0, 0.33]$) and the extrapolation regime ($t \in [0.33, 1]$), for all frameworks. Corresponding error plots are presented in Figure 7.